

Important Notice to Authors

No further publication processing will occur until we receive your response to this proof.

Attached is a PDF proof of your forthcoming article in PRB. Your article has 13 pages and the Accession Code is **BS13900**.

Please note that as part of the production process, APS converts all articles, regardless of their original source, into standardized XML that in turn is used to create the PDF and online versions of the article as well as to populate third-party systems such as Portico, Crossref, and Web of Science. We share our authors' high expectations for the fidelity of the conversion into XML and for the accuracy and appearance of the final, formatted PDF. This process works exceptionally well for the vast majority of articles; however, please check carefully all key elements of your PDF proof, particularly any equations or tables.

Figures submitted electronically as separate files containing color appear in color in the online journal. However, all figures will appear as grayscale images in the print journal unless the color figure charges have been paid in advance, in accordance with our policy for color in print (<https://journals.aps.org/authors/color-figures-print>).

Specific Questions and Comments to Address for This Paper

- 1 Please check change to M. A. R. Griffith.
- 2 Please note that the use of "novel" in this context is discouraged as it could lead to priority claims.
- 3 Please check changes. Use of the "first time" in this context also could result in a claim of priority.
- 4 Please note that Refs. [59–64] have not been cited. Please cite as appropriate, in consecutive order.
- 5 Please check we have set "... contributed equally..." statement as per style.
- 6 Please provide volume number for Ref. [53].
- 7 Please provide page no. in Ref. [59].

FQ: This funding provider could not be uniquely identified during our search of the FundRef registry (or no Contract or Grant number was detected). Please check information and amend if incomplete or incorrect.

Q: This reference could not be uniquely identified due to incomplete information or improper format. Please check all information and amend if applicable.

ORCIDs: Please follow any ORCID links (🟡) after the author names and verify that they point to the appropriate record for each author.

Open Funder Registry: Information about an article's funding sources is now submitted to Crossref to help you comply with current or future funding agency mandates. Crossref's Open Funder Registry (<https://www.crossref.org/services/funder-registry/>) is the definitive registry of funding agencies. Please ensure that your acknowledgments include all sources of funding for your article following any requirements of your funding sources. Where possible, please include grant and award ids. Please carefully check the following funder information we have already extracted from your article and ensure its accuracy and completeness:

Capes (BR)

Other Items to Check

- Please note that the original manuscript has been converted to XML prior to the creation of the PDF proof, as described above. Please carefully check all key elements of the paper, particularly the equations and tabular data.
- Title: Please check; be mindful that the title may have been changed during the peer-review process.
- Author list: Please make sure all authors are presented, in the appropriate order, and that all names are spelled correctly.
- Please make sure you have inserted a byline footnote containing the email address for the corresponding author, if desired. Please note that this is not inserted automatically by this journal.
- Affiliations: Please check to be sure the institution names are spelled correctly and attributed to the appropriate author(s).
- Receipt date: Please confirm accuracy.
- Acknowledgments: Please be sure to appropriately acknowledge all funding sources.
- Hyphenation: Please note hyphens may have been inserted in word pairs that function as adjectives when they occur before a noun, as in "x-ray diffraction," "4-mm-long gas cell," and "R-matrix theory." However, hyphens are deleted from word pairs when they are not used as adjectives before nouns, as in "emission by x rays," "was 4 mm in length," and "the R matrix is tested."

Note also that Physical Review follows U.S. English guidelines in that hyphens are not used after prefixes or before suffixes: superresolution, quasiequilibrium, nanoprecipitates, resonancelike, clockwise.

- Please check that your figures are accurate and sized properly. Make sure all labeling is sufficiently legible. Figure quality in this proof is representative of the quality to be used in the online journal. To achieve manageable file size for online delivery, some compression and downsampling of figures may have occurred. Fine details may have become somewhat fuzzy, especially

in color figures. The print journal uses files of higher resolution and therefore details may be sharper in print. Figures to be published in color online will appear in color on these proofs if viewed on a color monitor or printed on a color printer.

- Please check to ensure that reference titles are given as appropriate.
- Overall, please proofread the entire *formatted* article very carefully. The redlined PDF should be used as a guide to see changes that were made during copyediting. However, note that some changes to math and/or layout may not be indicated.

Ways to Respond

- **Web:** If you accessed this proof online, follow the instructions on the web page to submit corrections.
- **Email:** Send corrections to prbproofs@aptaracorp.com
Subject: **BS13900** proof corrections
- **Fax:** Return this proof with corrections to +1.703.791.1217. Write **Attention:** PRB Project Manager and the Article ID, **BS13900**, on the proof copy unless it is already printed on your proof printout.

Machine learning topological phases in real space

N. L. Holanda*

*Integrated Quantum Materials, Cavendish Laboratory, University of Cambridge, J. J. Thomson Avenue,
Cambridge, CB3 0HE, United Kingdom
and Centro Brasileiro de Pesquisas Físicas Rua Dr. Xavier Sigaud, 150-Urca, 22290-180, Rio de Janeiro, RJ, Brazil*

M. A. R. Griffith†

*Centro Brasileiro de Pesquisas Físicas, Rua Dr. Xavier Sigaud, 150-Urca, 22290-180, Rio de Janeiro, RJ, Brazil
and Departamento de Ciências Naturais, Universidade Federal de São João Del Rei, Praça Dom Helvécio 74, 36301-160,
São João Del Rei, MG, Brazil*



(Received 7 May 2020; accepted 10 August 2020; published xxxxxxxxxx)

We develop a supervised machine learning algorithm that is able to learn topological phases of finite condensed-matter systems from bulk data in real lattice space. The algorithm employs diagonalization in real space together with any supervised learning algorithm to learn topological phases through an eigenvector ensembling procedure. We combine our algorithm with decision trees and random forests to successfully recover topological phase diagrams of Su-Schrieffer-Heeger (SSH) models from bulk lattice data in real space and show how the Shannon information entropy of ensembles of lattice eigenvectors can be used to retrieve a signal detailing how topological information is distributed in the bulk. We further use insights obtained from these information entropy signatures to engineer global topological features from real-space lattice data that still carry most of the topological information in the lattice, while greatly diminishing the size of feature space, thus effectively amounting to a topological lattice compression. Finally, we explore the theoretical possibility of interpreting the information entropy topological signatures in terms of emergent information entropy wave functions, which lead us to Heisenberg and Hirschman uncertainty relations for topological phase transitions. The discovery of Shannon information entropy signals associated with topological phase transitions from the analysis of data from several thousand SSH systems illustrates how model explainability in machine learning can advance the research of exotic quantum materials with properties that may power future technological applications such as qubit engineering for quantum computing.

DOI: 10.1103/PhysRevB.00.004100

I. INTRODUCTION

The quest for innovative materials that harness exotic quantum properties has lured physicists into the realm of topological insulators and topological states of matter [1]. These materials feature previously unthought-of traits like bulk insulation coupled with metallic conductance at the surface and the splitting of currents according to spin orientation. Adding to that, these properties are protected by nontrivial topology that renders them robust to many sources of perturbation like thermal noise. Such characteristics make them promising candidates to being the cornerstone of 21st century technologies like spintronics and quantum computing.

These new topological states of matter have been studied in several contexts in condensed-matter physics including superconductors [2–5], ultracold atoms [6–10], photonic crystals [11–13], photonic quantum walks [14–16], and Weyl semimetals [17,18]. Among these, the Su-Schrieffer-Heeger (SSH) model [19] has attracted particular theoretical interest due to its simplicity and generality.

The SSH model is the simplest tight-binding model that exhibits a topological phase transition. As such, it can be viewed as the *Drosophila* of the field, providing a simple framework for testing new techniques. The model can be expressed in terms of creation and annihilation operators by the Hamiltonian

$$\mathbf{H}(\mathbf{t}) = \mathbf{c}^\dagger \mathbf{H}(\mathbf{t}) \mathbf{c} \quad (1)$$

and describes, e.g., the hopping of electrons along a one-dimensional chain comprising two atoms per unit cell (a brief discussion of the SSH model and its topological properties can be found in the Supplemental Material [20]). The SSH model has found several interesting applications in the modeling of diverse systems with nontrivial topology like optical lattices [21], polymeric materials [22], and topological mechanisms [23,24].

Many recent papers have explored the possibility of treating the general problem of determining phase transition boundaries of physical systems as machine learning tasks [25–41]. In the particular case of topological phase transitions, the usual approach for supervised learning is to generate a data set $(H_1(k), W_1), \dots, (H_n(k), W_n)$ whose inputs are representations of Hamiltonians in wave-vector space $H_i(k)$ and targets are their corresponding topological invariants W_i

*Corresponding author: linneuholanda@gmail.com, linneu@cbpf.br

†griffithphys@gmail.com

(for the SSH model the topological invariant is the winding number). Our paper extends this task to the case of learning topological phase diagrams from input data in real space. Strikingly, we find that information localized on a few lattice sites in the bulk is sufficient to predict with high accuracy which topological phase a particular Hamiltonian belongs to.

The main motivation for developing a data-driven approach based on real space is that the canonical method of choice for the analysis of topological systems, i.e., wave-vector space computations of topological invariants, is often only feasible for systems with translational symmetry, which many physical systems of current interest (e.g., disordered systems in condensed matter) do not have. Furthermore, it is not always granted that the topological invariants of a physical system being investigated are known in advance, as is presently the case for many gapless insulators. In such cases, being able to engineer topological features that encode the topological states of a system while at the same time reducing the system's complexity may provide an alternative strategy. Moreover, since real-space and wave-vector space eigenvectors are related by Fourier transforms, the latter are essentially delocalized and therefore so is any information recovered from them. Constructing theoretical methods to trace the distribution of information in topological systems may be an essential prerequisite to discovering new topological invariants and features. The data-driven approach designed in this paper addresses these issues.

To investigate topological phases of matter in real space, we have designed a supervised learning algorithm (here called eigenvector ensembling algorithm) tailored for the task of learning phase transition boundaries from local features. The algorithm is based on eigenvector decomposition and eigenvector ensembling and therefore will require minimal changes to be applicable to a broader class of data-driven physics problems. We describe the algorithm in detail in Sec. II and demonstrate its effectiveness by combining it with decision trees and random forests to recover the topological phase diagrams of SSH systems from local coordinates of eigenstates in real space. This is performed in Sec. III.

The advantage of using decision-tree-based algorithms to learn topological phases from local eigenvector data is that their use of entropy-based cost functions (such as Shannon information entropy or Gini impurity) furnishes them with an intrinsic model explainability tool that summarizes how important each feature was to learning the desired patterns in the data. This makes it much easier to trace the localization of relevant information along the features of a data set. Here, we use the Shannon information entropy of ensembles of real-space eigenvectors to recover a signal quantifying the amount of topological information available from each lattice site. This is a highly nontrivial proposition since the topological phase of a system is a global property of the system as a whole emerging from complex interactions between its components, and therefore even defining a local topological signal is a daunting theoretical task. We present a signal describing the localization of topological information in the bulk of topological condensed matter systems. These topological signals, here called information entropy signatures, are the subject of Sec. IV.

In possession of the information entropy signatures, we demonstrate how the symmetries in real and wave-vector space eigenvectors can be manipulated with signal processing tools commonly employed in audio and image processing to execute two standard unsupervised learning tasks, namely, dimensionality reduction and feature engineering. The topological features resulting from this analysis, here denominated discrete cosine transform and discrete sine transform topological features, are discussed in Sec. V.

The information entropy signatures are finally explored as theoretical constructs in terms of information entropy mass functions along the lattices. By taking their continuum limit and admitting that they are quantum in nature, we show how the information entropy signatures can be naturally understood in terms of emergent information entropy wave functions along the lattices. The theoretical formulation of the results obtained with machine learning in terms of emergent quantum mechanical wave functions allows us to establish Heisenberg and Hirschman uncertainty principles for the localizability of information entropy in topological phase transitions. The emergent information entropy wave functions are the theme of Sec. VI.

The discovery of information entropy signatures of topological phase transitions and their description as a measurable emergent phenomenon originating from the information entropy of ensembles of topological systems proximal to phase transition boundaries provide clear illustrations of how model explainability in machine learning can guide new discoveries in condensed matter and quantum materials physics since the existence of these signals was established by analyzing data from several thousand SSH systems which, taken individually, could not have provided any concrete hint of their existence.

As of yet, model explainability [42–44] is one of the topics at the edge of machine learning research that has been little explored by the physics community working at the interface between the two disciplines. This raises important questions as to whether machine learning can in fact help to advance theoretical investigation in physics since the majority of physics papers published on the subject are proofs of concept aimed at showing that modern machine learning techniques are capable of recognizing the relevant patterns in data from physical systems whose properties were known in advance. By proposing concepts from the data analysis of physical systems of contemporary interest and knitting together ideas from topological phase transitions and information theory by dint of model explainability, we expect to draw the physics community's attention to this essential machine learning tool.

II. EIGENVECTOR ENSEMBLING ALGORITHM

The eigenvector ensembling algorithm consists of five steps: (1) generating Hamiltonians in real space and their corresponding winding numbers; (2) creating training, validation, and test sets; (3) training on real-space eigenvectors of Hamiltonians in the training set; (4) eigenvector ensembling, and (5) bootstrapping. We describe here in detail each of these steps as they were implemented in this work. For a comprehensive introduction to the concepts referenced in the steps below, we recommend Ref. [45].

(1) *Generating Hamiltonians and winding numbers.* We start generating a number of parametrized Hamiltonians $H(\mathbf{t})$ in real space and their corresponding winding numbers $W(\mathbf{t})$, where $\mathbf{t} = (t_1, t_2, \dots, t_h)$ is a vector of h hopping parameters (in the simplest case of the SSH model $h = 2$). These Hamiltonians are $N \times N$ matrices, where N is twice the number of unit cells in the chain.

(2) *Creating training, validation, and test sets.* We split our set of parametrized Hamiltonians and winding numbers into training, validation, and test sets, as is usually done in machine learning. More explicitly, assume our hopping parameter vector \mathbf{t} takes on the values $\mathbf{t}_1, \mathbf{t}_2, \dots, \mathbf{t}_n$ corresponding to the Hamiltonian-winding number pairs $(H_1, W_1), \dots, (H_n, W_n)$. We partition the set $\{(H_i, W_i) \mid i = 1, \dots, n\}$ in three disjoint subsets: the training set, the validation set, and the test set.

(3) *Training on eigenvectors in real space.* Since each Hamiltonian H_i is represented by an $N \times N$ matrix, each one will provide N eigenvectors $\mathbf{v}_i^{(1)}, \mathbf{v}_i^{(2)}, \dots, \mathbf{v}_i^{(N)}$ to our data set. Our supervised learning algorithm of choice will take as inputs the real-space eigenvectors $\mathbf{v}_i^{(j)}$ of each Hamiltonian H_i in the training set and be trained to learn the winding number W_i of their parent Hamiltonian H_i . Therefore, our data set will consist of eigenvector-winding number pairs $(\mathbf{v}_i^{(j)}, W_i)$.

(4) *Eigenvector ensembling.* In order to predict the phase of a system described by a particular Hamiltonian, we need to take into account how each of its eigenvectors were classified. This amounts to performing ensemble learning on the eigenvectors of each Hamiltonian. In this work we estimate the phase probabilities for each Hamiltonian as the fraction of its eigenvectors that were classified in each phase.

(5) *Bootstrapping.* We refine the phase probabilities for each Hamiltonian using a bootstrapping procedure, i.e., we repeat steps (1)–(4) n_{expt} times, at each round sampling randomly a new training set from our grid in \mathbf{t} space. The final estimated probabilities are then arrived at by averaging the probabilities obtained in each experiment.

Before continuing to the analyses of the SSH systems with the eigenvector ensembling algorithm, it will be timely to digress a moment and peek into the algorithm itself. The focus on eigenvectors (and hence the algorithm's name) as the input data to a machine learning algorithm of choice is a hallmark of the procedure as it differentiates it from related applications of machine learning to the study of phase transitions. The intuition that eigenvectors can be used in replacement of raw Hamiltonians can be grasped when we consider the spectral decomposition of a Hamiltonian H :

$$H = \sum_{i=1}^N \lambda^{(i)} |\mathbf{v}^{(i)}\rangle \langle \mathbf{v}^{(i)}|, \quad (2)$$

where $\lambda^{(i)}$ is the eigenenergy corresponding to the eigenstate $|\mathbf{v}^{(i)}\rangle$. It is therefore clear that all information available from a Hamiltonian can be recovered from its spectral decomposition. By expressing the eigenvectors in a basis suitable to a particular problem (e.g., the real-space basis chosen in this paper), it becomes possible to investigate the properties of a set of Hamiltonians using the coordinates of eigenvectors in the chosen basis as features. Thus, the eigenvector ensembling procedure described above provides a broad framework for

the implementation of model explainability in applications to data-driven physics.

III. NUMERICAL EXPERIMENTS

We performed two numerical experiments with the eigenvector ensembling algorithm. The first experiment deals with the simplest case, the SSH model with nearest-neighbor hopping [here called SSH 1, Fig. 1(a)], while the second experiment uses the SSH model with first- and second-nearest-neighbor hoppings [here called SSH 2, Fig. 1(b)].

In each experiment our grid consisted of 6561 Hamiltonians uniformly distributed in the closed square $[-2, 2] \times [-2, 2]$ in the t_1 - t_2 plane in parameter space. The goal in each experiment is to recover the corresponding phase diagram in 2D (two-dimensional) parameter space [Figs. 1(a) and 1(b)] from local lattice data in the much higher-dimensional real space (100 D, in both experiments lattices have 50 unit cells, yielding 100×100 Hamiltonian matrices).

This task is particularly hard near phase transition boundaries, where numerical computation of winding numbers becomes less stable. For this reason, when sampling the training set we only consider those Hamiltonians in the grid whose numerically computed winding numbers lie in a minimum range of $\epsilon = 0.01$ from the correct winding-number values. Therefore, a good performance metric is the accuracy measured at those Hamiltonians near phase transitions that are never used for training, and thus we assign them to the test set. The remaining Hamiltonians in the grid are split into training and validation sets as detailed in the sections below.

As performance metrics, we report here both accuracy of predicted classes for eigenvectors as well as accuracy of predicted classes for Hamiltonians obtained from eigenvector ensembling. These accuracy scores are to be gauged against the baseline of a system that simply guesses the most frequent class for all Hamiltonians. Checking against this baseline is important because it indicates whether the decision trees are in fact learning the underlying patterns that relate real-space coordinates to winding numbers, and therefore whether the associated information entropy signature is meaningful or not.

When generating the Hamiltonians we applied periodic boundary conditions to eliminate border effects. This should make recovering a topological signal from local eigenvector coordinates even harder since, in this case, the translational symmetry of the systems should allow for no obvious way to distinguish between unit cells. The choice of periodic boundary conditions also implies that the information recovered from real-space data comes from the bulk of the topological systems considered and therefore provides strong evidence for the existence of topological signatures in the bulk of such systems.

Figures 2 and 3, respectively, illustrate single iterations of experiment 1 (Sec. III A) and experiment 2 (Sec. III B) as seen from parameter space. The accuracy statistics presented in the following subsections, as well as the probability heat maps and recovered phase diagrams shown in Figs. 4 and 5 were obtained after bootstrapping each experiment $n_{\text{expt}} = 100$ times. Thus, each probability heat map shown in Figs. 4(a), 4(b) and 5(a)–5(d) represents the averaged

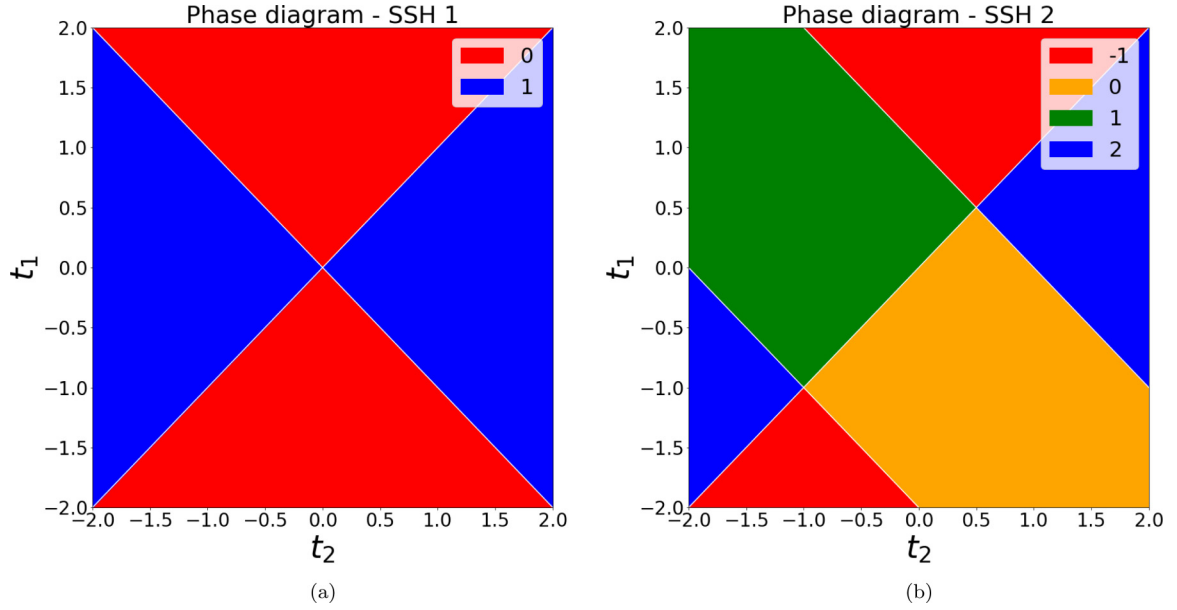


FIG. 1. Phase diagrams in parameter space. (a) SSH model with first-neighbor hoppings t_1 and t_2 . The (red) regions with winding number $W = 0$ are trivial, while the (blue) regions with winding number $W = 1$ are topologically nontrivial. (b) SSH model with first (t_1 and t_2) and second (T_1 and T_2) nearest-neighbor hoppings. In this paper we set $t_1 = t_2 = 1$ and renamed the variables $T_1 \rightarrow t_1$, $T_2 \rightarrow t_2$ for convenience. The (orange) region with winding number $W = 0$ is trivial while the others with winding numbers $W = -1$, $W = 1$, and $W = 2$ (red, green, and blue respectively) are topologically nontrivial.

fraction of eigenvectors of each Hamiltonian in the grid that were classified with a given winding number across 100 experiments. The recovered phase diagrams 4(c) and 5(d) are constructed by superposing the corresponding probability heat maps. As these figures make clear, the recovered phase diagrams faithfully portray the true phase diagrams in Fig. 1, with clear phase transition lines appearing in the regions of highest uncertainty.

The numerical experiments with the eigenvector ensemble algorithm described in the next subsections were implemented in Python using the SCIKIT-learn module [46,47].

A. Experiment 1: Learning a first-neighbor hopping SSH model with decision trees

Our test set in this experiment contained 1005 Hamiltonians (approximately 15.32% of all data). Of the remaining 5556 Hamiltonians, 556 were randomly assigned to the training set (approximately 8.47%) and 5000 (approximately 76.21%) were used to compute validation scores at each iteration. These proportions between training and validation sets are such that approximately 10% of Hamiltonians from outside of the test set were used for training at each iteration. The composition of the train + validation set for this

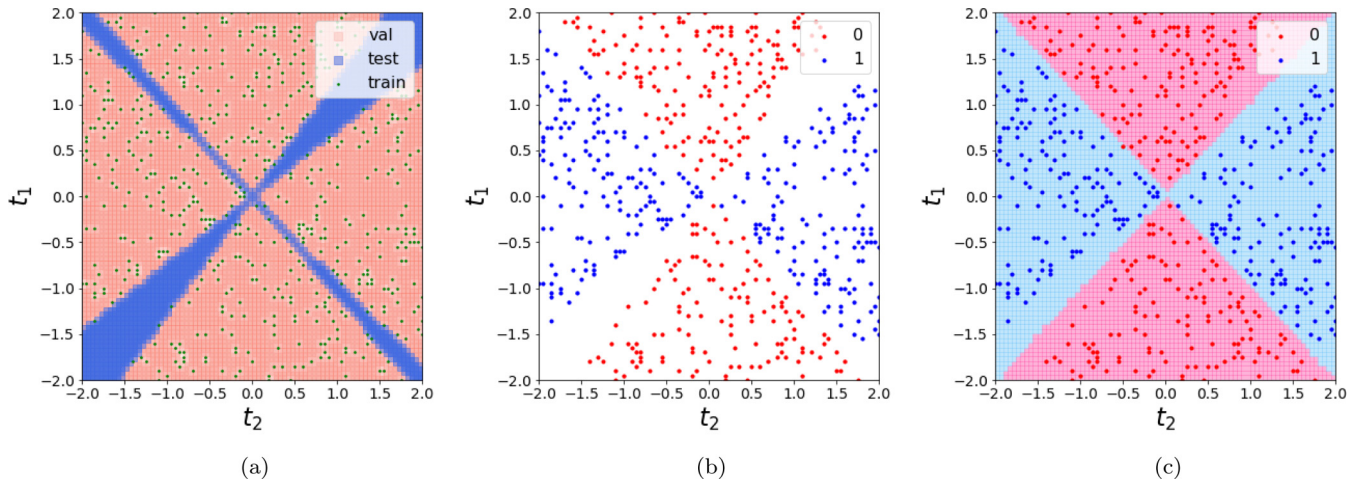


FIG. 2. Visualization of a single iteration of experiment 1 (Sec. III A) as seen from 2D parameter space. (a) Train/validation/test split. (b) Distribution of winding numbers in the training set. (c) Phase diagram learned from real-space lattice data by combining a decision tree with eigenvector ensembling.

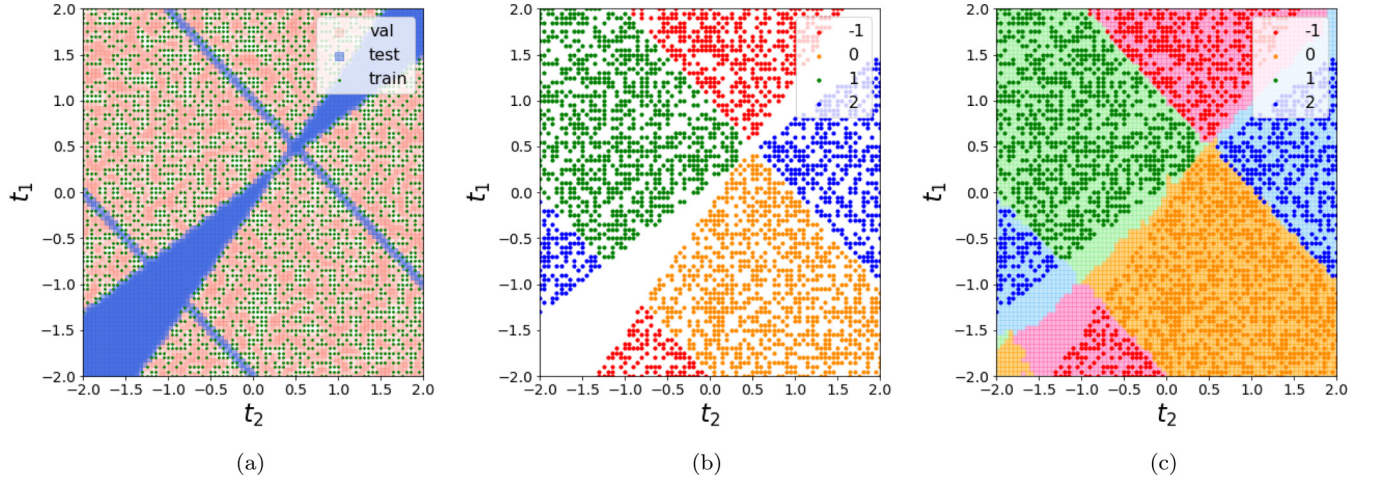


FIG. 3. Visualization of a single iteration of experiment 2 (Sec. III B) as seen from 2D parameter space. (a) Train/validation/test split. (b) Distribution of winding numbers in the training set. (c) Phase diagram learned from real-space lattice data by combining a random forest with eigenvector ensembling.

experiment was 50.79% of Hamiltonians with winding number $W = 0$ and 49.21% with winding number $W = 1$. The composition of the test set was 44.79% of Hamiltonians with winding number $W = 0$ and 55.21% with winding number $W = 1$. Our learning algorithm of choice for this experiment was a simple decision-tree model [48].

The bootstrap allows us to collect several statistics to evaluate performance. In particular, we report mean accuracies on training eigenvectors (0.9814), validation eigenvectors (0.9639), and test eigenvectors (0.7897). Eigenvector ensembling substantially improved mean accuracies for Hamiltonians. These were 1.000 for training Hamiltonians, 1.000 for validation Hamiltonians, and 0.9919 for test Hamiltonians. When compared with the baseline test accuracy of 0.5521 of a system that predicts the whole test set as having winding number $W = 1$, the accuracy achieved on test Hamiltonians

indicates that the decision trees indeed learned the patterns that relate real-space coordinates to winding numbers.

The probability heat maps and phase diagram learned by the combination of decision trees with eigenvector ensembling used in experiment 1 are shown in Fig. 4.

B. Experiment 2: Learning a first- and second-neighbor hopping SSH model with random forests

This task is considerably more difficult than the previous one due to the higher number of classes and the fact that some of the labels encompass disconnected regions. For this reason, instead of using a single decision tree, we upgraded our model to a random forest [49] with 25 decision trees. Our data set consisted of 1040 (15.85%) test Hamiltonians. The remaining 5521 Hamiltonians are randomly split in half

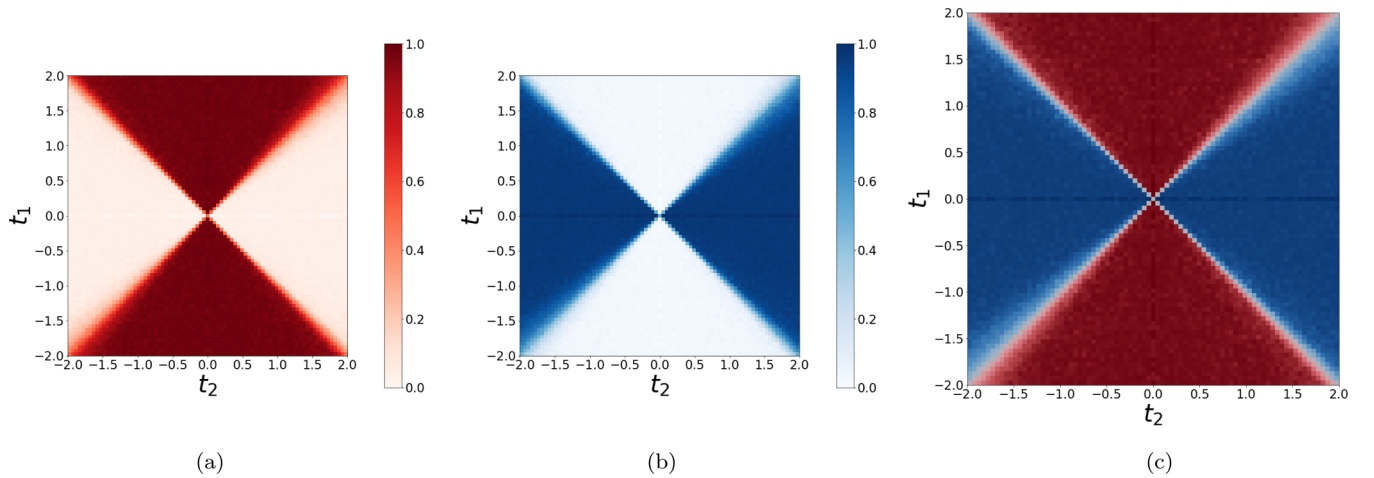


FIG. 4. Probability heat maps learned by a combination of decision trees with eigenvector ensembling from bulk real-space eigenvector data in experiment 1 (Sec. III A). Heat maps were averaged across all 100 iterations of the experiment. (a) Probability heat map showing the probability that a Hamiltonian in the grid has winding number equal to 0. (b) Probability heat map showing the probability that a Hamiltonian in the grid has winding number equal to 1. (c) The phase diagram resulting from heat maps (a) and (b).

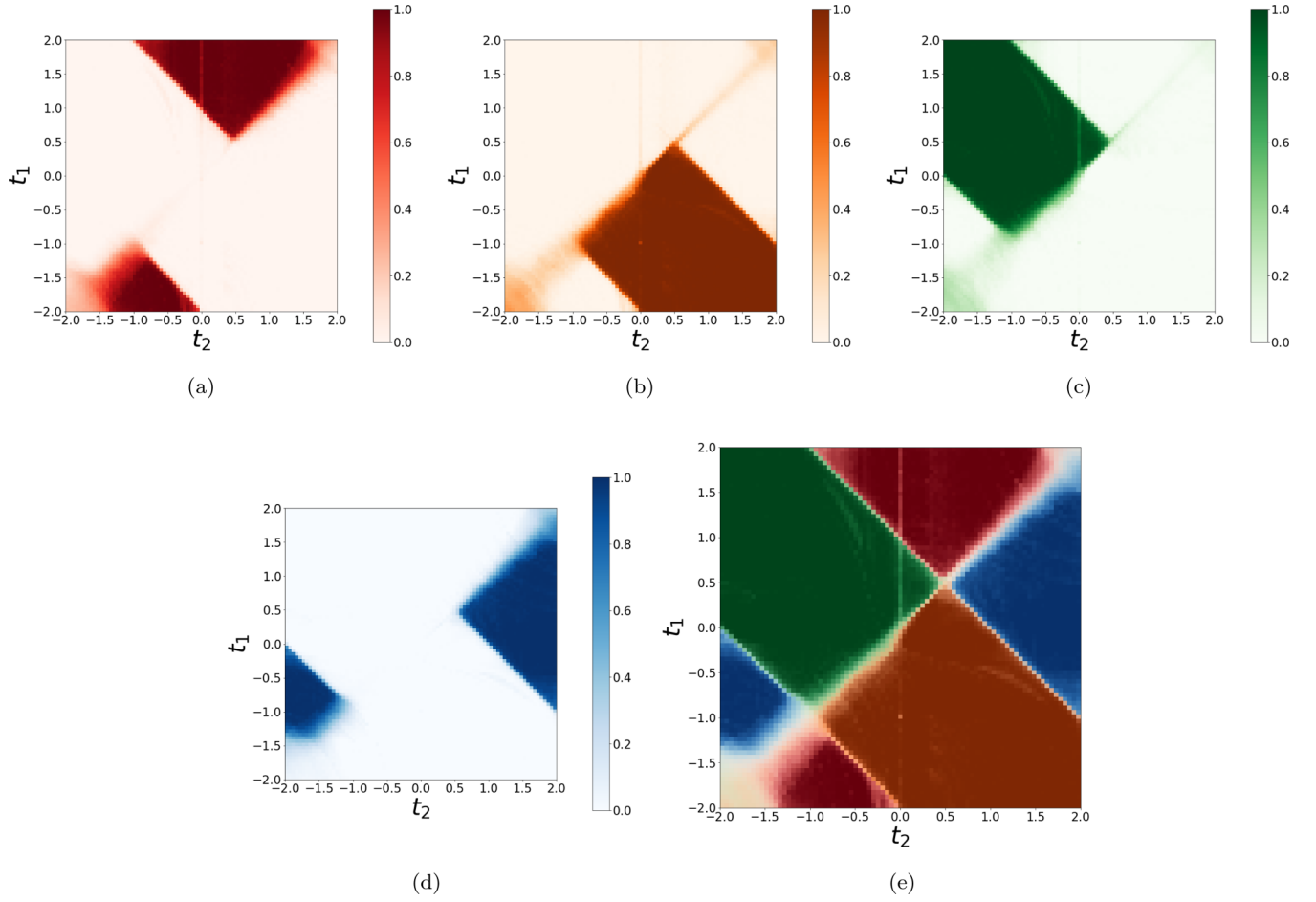


FIG. 5. Probability heat maps learned by a combination of random forests with eigenvector ensembling from bulk real-space eigenvector data in experiment 2 (Sec. III B). Heat maps were averaged across all 100 iterations of the experiment. (a) Probability heat map showing the probability that a Hamiltonian in the grid has winding number equal to -1 . (b) Probability heat map showing the probability that a Hamiltonian in the grid has winding number equal to 0 . (c) Probability heat map showing the probability that a Hamiltonian in the grid has winding number equal to 1 . (d) Probability heat map showing the probability that a Hamiltonian in the grid has winding number equal to 2 . (e) The phase diagram resulting from heat maps (a)–(d).

between training and validation sets at each iteration, giving 2761 (42.08%) training Hamiltonians and 2760 (42.07%) validation Hamiltonians. The distribution of winding numbers for the Hamiltonians in the train + validation set for this experiment was $W = -1$ (17.90%), $W = 0$ (32.51%), $W = 1$ (32.26%), and $W = 2$ (17.33%). The distribution of winding numbers for the Hamiltonians in the test set was $W = -1$ (36.32%), $W = 0$ (11.06%), $W = 1$ (12.69%), and $W = 2$ (39.93%).

Mean accuracies across 100 repetitions of experiment 2 were 0.9997 for training eigenvectors, 0.9709 for validation eigenvectors, and 0.6634 for test eigenvectors. Mean accuracies resulting from eigenvector ensembling were 1.000 for training Hamiltonians, 0.9972 for validation Hamiltonians, and 0.8797 for test Hamiltonians. The large accuracy gain achieved by eigenvector ensembling in the test set (going from 0.6634 eigenvector accuracy to 0.8797 Hamiltonian accuracy) attests to its power. The effectiveness of eigenvector ensembling is also evident from the much worse performance (0.3993) achieved by a baseline system that simply guesses $W = 2$ for all test Hamiltonians in this experiment.

The probability heat maps and phase diagram learned by the combination of random forests with eigenvector ensembling used in experiment 2 are shown in Fig. 5.

IV. INFORMATION ENTROPY SIGNATURES

We now analyze how the algorithm was able to recover a global property of the Hamiltonians (their topological phase) from bulk local features (real-space eigenvector coordinates on each lattice site). Alongside the fact that decision trees and random forests are very easy to train and visualize, the other reason that led us to test the eigenvector ensembling algorithm with them was that they allow us to check which features (and thus which lattice sites) were most informative in training.

The (normalized) relevance of a feature is given by how much it reduces a loss function (in this paper, the Shannon information entropy of ensembles of eigenvectors). By averaging normalized relevances as measured by reduction in the information entropy of ensembles of real-space eigenvectors across $n_{\text{expt}} = 100$ iterations of both experiment 1 (Sec. III A) and experiment 2 (Sec. III B) we recovered

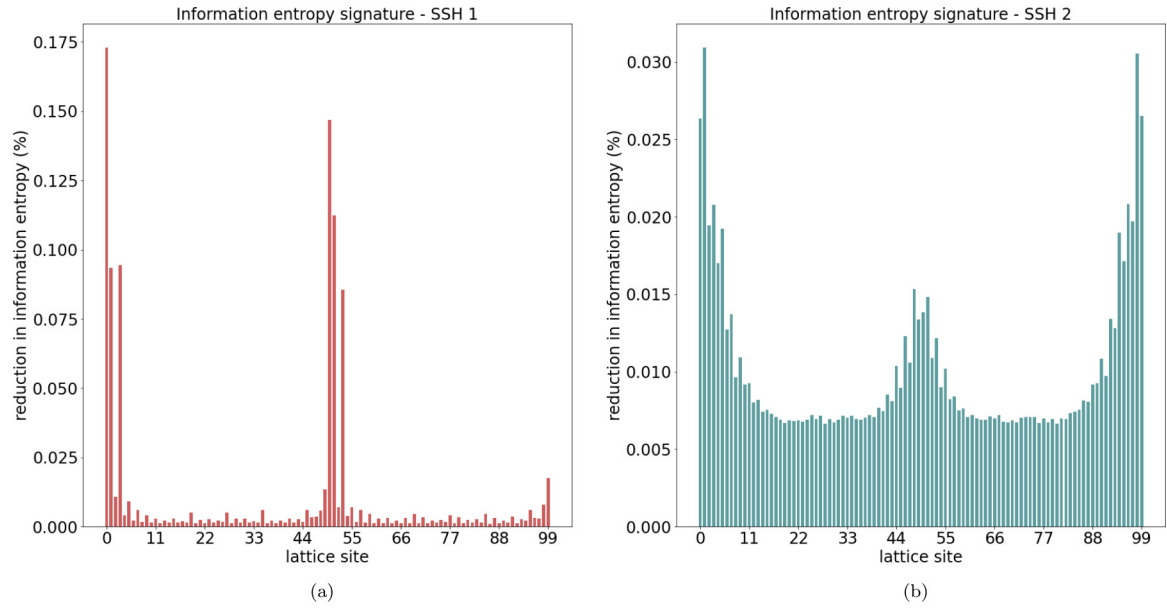


FIG. 6. Information entropy signatures of the topological phase transitions from the numerical experiments of Sec. III. (a) In experiment 1 (Sec. III A), the two sharp peaks in the Shannon entropy signal account for approximately 70% of reduction in information entropy. (b) In experiment 2 (Sec. III B), the three visible peaks account for approximately 30% of reduction in information entropy.

Shannon entropy signals that reveal which lattice sites were consistently more relevant in learning topological phases from data in real space for each experiment. These signals are the information entropy signatures of each topological phase transition.

We should briefly comment on the possibility of using the Gini impurity of ensembles of eigenvectors [45] instead of their Shannon entropy as cost function. This would similarly lead us to Gini impurity signatures of topological phase transitions. Given that in the examples analyzed in this paper the Gini impurity signatures and the Shannon entropy signatures were very similar, the larger familiarity of a general physics audience with the latter influenced us to choose it over the former. Nevertheless, the question of which split criterion should be used when training decision trees is as of yet largely undecided [50] and may be of relevance in the analysis of other physical systems than the ones studied here.

The bar plots in Fig. 6 show how informative each lattice site was in learning topological phases for each experiment. They represent the information entropy signatures along the lattices in each SSH system. For experiment 1 (Sec. III A), only six lattice sites (0, 1, 3, 50, 51, 53) corresponding to the two sharp peaks seen in Fig. 6(a) contributed approximately 70% of total reduction in Shannon entropy. Similarly, approximately 30% of total reduction in the Shannon information entropy of eigenvector data from experiment 2 (Sec. III B) was achieved by 18 lattice sites (0, 1, 2, 3, 4, 5, 46, 48, 49, 50, 51, 53, 94, 95, 96, 97, 98, 99) distributed along the three peaks in Fig. 6(b). As we shall see in Sec. V, the information entropy signatures can be used to compress the topological information in SSH lattices.

The information entropy signatures presented here have some interesting subtleties. Although they give us a visualization of how important each lattice site was in determining

the topological phases of Hamiltonians, they actually express a global property of the whole lattice. In Sec. VI, where we develop a quantum formalism for the information entropy signatures obtained in this section, these seemingly antagonistic conceptions shall be harmonized. What is important to emphasize at this point is that an information entropy signature should not be naively taken at face value: a lattice site that appears unimportant in an information entropy signature plot may not be unimportant or void of topological information by itself.

To give a concrete example, reduction in Shannon entropy tends to be distributed among highly correlated variables. This implies that if only a single lattice site in a highly correlated subset is used by a learning algorithm, it will likely inherit most of the reduction in Shannon entropy from the other correlated lattice sites that were not taken into account by the algorithm. The corollary of this fact is that lattice sites that carry redundant information that is also available from other lattice sites tend to have decreased importance in the information entropy signature. In this regard, the information entropy signatures presented here express a summary of relations between lattice sites and are therefore intrinsically global.

Each of the information entropy signatures shown in Fig. 6 captures a general pattern that persists regardless of the length of the lattice (i.e., the number of unit cells) used to compute them. In fact, by rerunning each experiment with longer lattices we have verified that the signals in Figs. 6(a) and 6(b) appear to converge to well-defined continuous density functions in the macroscopic limit. They are not, therefore, artifacts of particular choices of hyperparameters used to run the eigenvector ensembling algorithm. The information entropy signatures for longer lattices are presented in the Supplemental Material [20].

V. TOPOLOGICAL FEATURE ENGINEERING AND LATTICE COMPRESSION

In this section, we explore the information entropy signatures obtained in Sec. IV from a signal processing perspective. As we shall see, this will enable us to perform two important unsupervised learning tasks on topological systems: dimensionality reduction and data compression.

As a cursory glance at Figs. 6(a) and 6(b) seems to suggest, the existence of peaks and symmetries in information entropy signatures can be exploited as a powerful dimensionality reduction tool: by keeping only the most relevant lattice sites in an information entropy signature, the amount of data needed to characterize the topological phase of a SSH system can be largely decreased with little loss of information. Nevertheless, given that the topological phase of a SSH system is a global property of the whole lattice, it is natural to expect that it should be possible to engineer global features from real-space coordinates. Here, we show how the symmetries in real-space eigenvectors and information entropy signatures can be exploited to engineer new global topological features, leading to an effective compression of topological information.

Given a real-space eigenvector $x[m]$, we can compute its coordinates in wave vector space using the discrete Fourier transform (DFT)

$$\hat{x}[n] = \frac{1}{\sqrt{N}} \sum_{m=0}^{N-1} x[m] e^{-i \frac{2\pi}{N} nm}, \quad n = 0, \dots, N-1. \quad (3)$$

Since the choice of phase of the real-space eigenvectors was such that they were all in \mathbb{R}^N , the eigenvectors in wave-vector space computed from Eq. (3) will be Hermitian vectors in \mathbb{C}^N . The Hermitian symmetry of the wave-vector space eigenvectors manifests itself mathematically in closed lattices with periodic boundary conditions as

$$\hat{x}[\bar{k}] = \hat{x}^*[\overline{N-k}], \quad k = 0, \dots, N-1 \quad (4)$$

where we have used the notation $\bar{k} = k \bmod N$.

Equation (4) forks into two natural paths to topological feature engineering. In the first path, we exploit the fact that the real part of $\hat{x}[m]$ is even symmetric around the reciprocal lattice sites 0 and $\frac{N}{2}$. This leads us to the discrete cosine transform (DCT) topological features

$$\hat{x}^c[n] = x[0] + (-1)^n x[M-1] + \sum_{m=1}^{M-2} 2x[m] \cos\left(\frac{\pi}{M-1} nm\right), \quad n = 0, \dots, M-1 \quad (5)$$

where $M = \frac{N}{2} + 1$. The second path capitalizes on the fact that the imaginary part of $\hat{x}[m]$ is odd symmetric around the reciprocal lattice sites 0 and $\frac{N}{2}$, thus yielding the discrete sine transform (DST) topological features

$$\hat{x}^s[n] = \sum_{m=0}^{M-1} 2x[m+1] \sin\left(\frac{\pi}{M+1} (n+1)(m+1)\right), \quad n = 0, \dots, M-1 \quad (6)$$

where $M = \frac{N}{2} - 1$.

The topological features in both Eqs. (5) and (6) are generated from only half of the real-space lattice, i.e., the sites

$0 \leq l \leq \frac{N}{2}$. This is due to the fact that each equation assumes that the eigenvectors are even symmetric (DCT topological features) or odd symmetric (DST topological features) around the lattice sites 0 and $\frac{N}{2}$ in real space as well. While these assumptions are strictly true for the eigenvector representations in wave-vector space, they are not generally true for the real-space representations. Therefore, Eqs. (5) and (6) achieve lattice compression by keeping only half of the real-space eigenvector coordinates and imposing the corresponding boundary conditions (even symmetry or odd symmetry) on the lattice sites 0 and $\frac{N}{2}$ to extrapolate the information from one half of the lattice to the other.

The topological feature engineering techniques described above are commonly employed in several applications of digital signal processing like audio and image processing and, most importantly here, data compression. As Eqs. (4)–(6) show, signal transforms such as the DCT and DST profit from the redundancy of information arising from the existence of certain symmetries in signals, allowing us to write a signal of length N in terms of at most $M = \frac{N}{2} + 1$ features.

We ran several numerical experiments to evaluate if the DCT and DST topological features defined in Eqs. (5) and (6) are able to efficiently encode the topological information existing in SSH lattices. The accuracy scores obtained in each experiment are listed in Table I, where we also report the accuracy scores of the numerical experiments of Sec. III.

The lattice compression strategies tested in this work were as follows: (i) learning topological phases from only a subset of real-space lattice sites; (ii) learning topological phases from the DCT or DST engineered features of Eqs. (5) and (6); (iii) learning topological phases from a fraction of the DCT or DST topological features; and (iv) learning topological phases from a fraction of the DCT or DST features, computed from only a fraction of real-space lattice sites.

In strategy (i) the lattice sites used in the SSH 1 and SSH 2 systems were

$$\begin{aligned} \mathcal{S}_1 &= (0, 1, 3, 50) \quad \text{and} \\ \mathcal{S}_2 &= (0, 1, 2, 3, 4, 5, 6, 7, 46, 48, 49, 50). \end{aligned} \quad (7)$$

Note that for the nearest-neighbor SSH systems \mathcal{S}_1 corresponds to the four most informative sites such that $0 \leq l \leq 50$ as indicated by the information entropy signature in Fig. 6(a). Similarly, for the first- and second-nearest-neighbor SSH systems \mathcal{S}_2 corresponds to the 12 most informative sites such that $0 \leq l \leq 50$ in the corresponding information entropy signature in Fig. 6(b). In Table I, the features used in strategy (i) are referred to as $X_{\mathcal{S}_1}$ and $X_{\mathcal{S}_2}$, according to the SSH systems they relate to. In strategy (ii), the full set of DCT or DST topological features written in Eqs. (5) and (6) were used. These features are denoted in Table I by \hat{X}_1^c , \hat{X}_1^s , \hat{X}_2^c , \hat{X}_2^s , according to which set of topological features and SSH systems they refer to.

Similarly to strategy (i), in strategy (iii) we selected the most informative DCT topological features of both SSH 1 and SSH 2 systems that were obtained from strategy (ii),

$$\begin{aligned} \mathcal{E}_1 &= (1, 2, 36, 49) \quad \text{and} \\ \mathcal{E}_2 &= (0, 1, 2, 3, 4, 5, 6, 7, 47, 48, 49, 50) \quad (\text{DCT}) \end{aligned} \quad (8)$$

TABLE I. Accuracy scores of numerical experiments. The features used to train the decision trees (SSH 1) or random forests (SSH 2) in the numerical experiments with SSH systems were as follows. Real-space features: all real-space lattice sites (X_α) (Secs. III A and III B); real-space lattice sites from subset \mathcal{S}_α ($X_{\mathcal{S}_\alpha}$) [Eq. (7)]. DCT topological features: all DCT topological features (\hat{X}_α^c) [Eq. (5)]; DCT topological features from subset \mathcal{E}_α ($\hat{X}_{\mathcal{E}_\alpha}^c$) [Eq. (8)]; DCT topological features from subset \mathcal{E}_α computed using only real-space lattice sites \mathcal{S}_α ($\hat{X}_{\mathcal{S}_\alpha, \mathcal{E}_\alpha}^c$) [Eq. (10)]. DST topological features: all DST topological features (\hat{X}_α^s) [Eq. (6)]; DST topological features from subset \mathcal{O}_α ($\hat{X}_{\mathcal{O}_\alpha}^s$) [Eq. (9)]; DST topological features from subset \mathcal{O}_α computed using only real-space lattice sites \mathcal{S}_α ($\hat{X}_{\mathcal{S}_\alpha, \mathcal{O}_\alpha}^s$) [Eq. (11)].

SSH system	Features	Val. eigenvectors	Test eigenvectors	Val. Hamiltonians	Test Hamiltonians
1	X_1	0.9639	0.7897	1.000	0.9919
1	$X_{\mathcal{S}_1}$	0.9444	0.7763	0.9853	0.9853
1	\hat{X}_1^c	0.9521	0.7374	0.9976	0.9916
1	$\hat{X}_{\mathcal{E}_1}^c$	0.8280	0.6067	0.9979	0.9191
1	$\hat{X}_{\mathcal{S}_1, \mathcal{E}_1}^c$	0.9444	0.8176	0.9853	0.9934
1	\hat{X}_1^s	0.9533	0.7314	0.9906	0.9856
1	$\hat{X}_{\mathcal{O}_1}^s$	0.6942	0.5420	0.7088	0.4798
1	$\hat{X}_{\mathcal{S}_1, \mathcal{O}_1}^s$	0.9456	0.7818	0.9854	0.9399
2	X_2	0.9709	0.6634	0.9972	0.8797
2	$X_{\mathcal{S}_2}$	0.9590	0.6168	0.9961	0.9961
2	\hat{X}_2^c	0.9740	0.6895	0.9976	0.8862
2	$\hat{X}_{\mathcal{E}_2}^c$	0.8990	0.5357	0.9955	0.7897
2	$\hat{X}_{\mathcal{S}_2, \mathcal{E}_2}^c$	0.8999	0.5030	0.9956	0.7671
2	\hat{X}_2^s	0.9735	0.6878	0.9971	0.8899
2	$\hat{X}_{\mathcal{O}_2}^s$	0.9042	0.5527	0.9918	0.7427
2	$\hat{X}_{\mathcal{S}_2, \mathcal{O}_2}^s$	0.8204	0.4127	0.9942	0.5903

and the most informative DST topological features of both systems that were obtained from strategy (ii) as well,

$$\mathcal{O}_1 = (0, 18, 28, 30) \quad \text{and}$$

$$\mathcal{O}_2 = (0, 1, 2, 3, 4, 5, 43, 44, 45, 46, 47, 48) \quad (\text{DST}). \quad (9)$$

The features in strategy (iii) are denoted in Table I by $\hat{X}_{\mathcal{E}_1}^c$, $\hat{X}_{\mathcal{O}_1}^s$, $\hat{X}_{\mathcal{E}_2}^c$, $\hat{X}_{\mathcal{O}_2}^s$, according to the topological features and wave-vector space subset used with each SSH system.

The most aggressive lattice compression strategy tested in this work was strategy (iv). It consists of using the DCT (DST) topological features of Eq. (8) [Eq. (9)], but having computed these topological features using only the real-space lattice sites given in Eq. (7). Thus, in strategy (iv) a lossy compression is performed both on real-space features and the engineered DCT (DST) topological features. Mathematically, we can express the topological features used in strategy (iv) as follows:

$$\begin{aligned} \hat{x}_{\mathcal{S}, \mathcal{E}}^c[n] &= \mathbb{1}_{\mathcal{S}}[0]x[0] + (-1)^n \mathbb{1}_{\mathcal{S}}[M-1]x[M-1] \\ &+ \sum_{m \in \mathcal{S}^*} 2x[m] \cos\left(\frac{\pi}{M-1}nm\right), \quad n \in \mathcal{E} \quad (\text{DCT}) \end{aligned} \quad (10)$$

$$\begin{aligned} \hat{x}_{\mathcal{S}, \mathcal{O}}^s[n] &= \sum_{m \in \mathcal{S}} 2x[m+1] \\ &\times \sin\left(\frac{\pi}{M+1}(n+1)(m+1)\right), \quad n \in \mathcal{O} \quad (\text{DST}) \end{aligned} \quad (11)$$

where in Eq. (10) the notation $\mathbb{1}_{\mathcal{S}}[l]$ stands for the indicator function of the lattice subset \mathcal{S} and \mathcal{S}^* is the complement of $\{0, M-1\}$ with respect to \mathcal{S} :

$$\mathbb{1}_{\mathcal{S}}[l] = \begin{cases} 1 & \text{if } l \in \mathcal{S}, \\ 0 & \text{otherwise,} \end{cases} \quad \mathcal{S}^* = \mathcal{S} \setminus \{0, M-1\}. \quad (12)$$

The features engineered in strategy (iv) are denoted in Table I by $\hat{X}_{\mathcal{S}_1, \mathcal{E}_1}^c$, $\hat{X}_{\mathcal{S}_1, \mathcal{O}_1}^s$, $\hat{X}_{\mathcal{S}_2, \mathcal{E}_2}^c$, $\hat{X}_{\mathcal{S}_2, \mathcal{O}_2}^s$, again referencing the type of topological features used, which components in real and wave-vector space engineered them and the appropriate SSH systems.

The results shown in Table I bring some startling surprises. For example, the topological phase transition boundaries of SSH 1 systems can be learned using only the four real-space lattice sites \mathcal{S}_1 with virtually no loss in accuracy, as seen from eigenvector and Hamiltonian accuracy scores for the features $X_{\mathcal{S}_1}$. The same appears to be true to SSH 2 systems, where the 12 real-space lattice sites \mathcal{S}_2 corresponding to the features $X_{\mathcal{S}_2}$ in the table produce accuracy scores at near the same level as using the whole lattice.

Even more striking is the performance achieved by the compressed DCT topological features $\hat{X}_{\mathcal{S}_\alpha, \mathcal{E}_\alpha}^c$ defined in Eq. (10). For SSH 1 systems, they perform on par with using the full set of real-space features X_1 , while for SSH 2 systems a small loss in accuracy is incurred relative to the full set of real-space features X_2 .

Another interesting insight comes from comparing the accuracy scores obtained with the DCT topological features versus the DST topological features. The latter have poorer performance than the former, as is indicated by the sharp

drops in accuracy scores obtained with the DST topological features in both SSH 1 and SSH 2 systems. This may be related to the fact that the odd-symmetric boundary conditions imposed on DST topological features imply discarding the lattice sites 0 and 50, which correspond to sharp peaks in the information entropy signatures of Figs. 6(a) and 6(b).

The accuracy scores obtained with the real-space features X_{S_α} and the DCT topological features $\hat{X}_{S_\alpha, \epsilon_\alpha}^\xi$, both of which use information from a small fraction of real-space lattice sites, demonstrate that learning topological phases from local real-space data in the bulk is still possible even for small subsets of lattice sites. In this sense, key topological information can be said to be localized on few sites in the lattice. We refer the reader to the Supplemental Material [20] for a discussion of how this is possible.

VI. EMERGENT INFORMATION ENTROPY WAVE FUNCTIONS

The information entropy signatures that we have been investigating pose an immediate theoretical question: How can a signal that is locally defined arise from a global property of the whole SSH lattice? In this section we venture into a theoretical exploration of the information entropy signatures in the hope of elucidating this issue. Our goal is to arrive at a theoretical framework that will allow us to interpret the information entropy signatures in terms of quantum mechanics.

We can think of the Shannon information entropy signatures in Figs. 6(a) and 6(b) as discrete information entropy mass functions that, in the continuum (i.e., macroscopic) limit of an infinite chain, lead to local entropy density functions along the lattices, which themselves become 1D manifolds. By mapping the lattice to a partition of the 1D manifold, the cumulative distribution of topological information in the continuum limit will be given by

$$F_S(x) = \int_{\ell}^{(x)} \rho_S(x') dx', \quad (13)$$

where $\rho_S(x)$ is the local information entropy density function in the continuum limit and x is defined by the coordinate system specified on the 1D manifold ℓ . The index S is meant to emphasize that in this paper we have used Shannon's definition of entropy to arrive at the information entropy signatures as opposed to, e.g., Gini impurity.

Our use of periodic boundary conditions implies that the coordinate x should be defined on the circle $S^1 = [0, 1]/R$, where R is the equivalence relation in $[0, 1]$ defining the circle S^1 ,

$$x R y \iff x = y \text{ or } (x, y) \in \{(0, 1), (1, 0)\}. \quad (14)$$

For open boundary conditions, the spatial coordinate x is defined on the closed interval $[0, 1]$ or, in the case of infinite systems, \mathbb{R} . However, for the sake of generality, we shall continue to use the calligraphic ℓ to denote an arbitrary 1D manifold in this section.

Given the quantum nature of the phase transitions being discussed, the information entropy density function $\rho_S(x)$ can be naturally interpreted as the squared magnitude of a spatial

information entropy wave function,

$$\rho_S(x) = |\psi_S(x)|^2, \quad (15)$$

the local density of topological information available from a single point in the 1D manifold then being expressed in bracket notation by Born's rule

$$\rho_S(x) = |\langle x | \psi_S \rangle|^2. \quad (16)$$

The counterpart of the spatial information entropy wave function $\psi_S(x)$ in wave-vector space is its Fourier transform

$$\hat{\psi}_S(k) = \int_{\ell} \psi_S(x) e^{-2\pi i k x} dx \quad (17)$$

from which the information entropy density function in wave-vector space can be computed:

$$\hat{\rho}_S(k) = |\hat{\psi}_S(k)|^2. \quad (18)$$

The interpretation of information entropy signatures in terms of information entropy wave functions opens several avenues of investigation of possible connections between exotic states of matter and quantum information theory. Here, we explore its most forthright corollary, which is the establishment of uncertainty relations for topological phase transitions.

Let us denote the mean, the variance, and the entropy associated with the probability distribution ρ_S by μ_{ρ_S} , $\sigma_{\rho_S}^2$, and H_{ρ_S} , respectively. Explicitly, we have

$$\mu_{\rho_S} = \int_{\ell} x \rho_S(x) dx, \quad (19a)$$

$$\sigma_{\rho_S}^2 = \int_{\ell} (x - \mu_{\rho_S})^2 \rho_S(x) dx, \quad (19b)$$

$$H_{\rho_S} = \int_{\ell} \rho_S(x) \ln(\rho_S(x)) dx, \quad (19c)$$

with analogous equations for the wave-vector space counterparts $\mu_{\hat{\rho}_S}$, $\sigma_{\hat{\rho}_S}^2$, and $H_{\hat{\rho}_S}$ in terms of $\hat{\rho}(k)$.

In possession of this quantum formalism, we may write topological versions of two canonical uncertainty relations that bind together the real space and wave-vector space information entropy density functions (15) and (18):

(i) *The Heisenberg uncertainty principle:*

$$\sigma_{\rho_S} \sigma_{\hat{\rho}_S} \geq \frac{1}{4\pi}. \quad (20)$$

(ii) *The Hirschman entropic uncertainty:*

$$H_{\rho_S} + H_{\hat{\rho}_S} \geq \ln\left(\frac{e}{2}\right). \quad (21)$$

The information entropy density function ρ_S devised in this section furnishes a physics-grounded interpretation of the information entropy signatures obtained in Sec. IV from sheer data analysis of finite SSH systems in real space. In particular, the uncertainty relations (20) and (21) express concisely the tradeoff between the localizability of information in topological phase transitions in real space and wave-vector space.

Perhaps the fundamental consequence of interpreting the information entropy density function $\rho_S(x)$ as the probability distribution resulting from an information entropy wave function $\psi_S(x)$ defined on a 1D manifold is that it reconciles the apparently conflicting notions of a local topological signal

arising from a global property of the SSH systems. Indeed, while $\psi_S(x)$ is defined locally at every point of the 1D manifold, it is a single, global wave function encoding the spatial distribution of topological information of an ensemble of SSH Hamiltonians close to phase transition boundaries in parameter space. Therefore, the information entropy wave function $\psi_S(x)$ and its corresponding information entropy density function $\rho_S(x)$ can be pictured as emergent properties of an ensemble of quantum many-body systems near phase transitions.

VII. DISCUSSION

Given the increasing complexity of systems studied in condensed-matter physics and the rising demand for materials with exotic and robust properties to power future technological progress, it is only expected that data-driven approaches to physics will grow in demand. Our work represents a step in this direction, as we have devised (Sec. II) and implemented (Sec. III) a data-driven approach to the discovery of previously unknown properties of topological materials from real-space data.

By starting from eigenvector data generated from the simulation of SSH systems in real space, proposing an approach based on eigenvector ensembling and decision trees and using model explainability to uncover the information entropy signatures presented in this paper, and then exploring the numerical and theoretical possibilities offered by the information entropy signatures, our work exemplifies a full cycle of data-driven physics and illustrates how the interactions between machine learning and physics can be enriching to both disciplines.

The development of data-driven methods based on real-space lattice data will be particularly relevant to the study of disordered systems in condensed matter. Such systems usually break translational symmetry and therefore are not amenable to canonical wave-vector space methods. Thus, the discovery and engineering of topological features from real-space data as demonstrated in this work carries great promise to the theoretical investigation of these systems.

Furthermore, as is generally the case in engineering, the evolution of quantum technologies such as quantum computing and quantum communication will likely depend on a delicate balance between simplicity and robustness of components such as topological qubits. On the simplicity side, engineers try to build their systems with as little redundancy as possible to reduce design complexity, while for robustness redundancy is a necessary commodity to ensure error correction within the system. We expect that information-theoretic approaches to quantum materials such as the one advanced by this paper shall eventually become a staple of quantum engineering.

As we have seen, the use of real-space data enabled us to investigate how topological information is spatially distributed in SSH systems. This was demonstrated by the information entropy signatures of Sec. IV, which were recovered from the Shannon entropy of ensembles of eigenvectors in each numerical experiment executed in Sec. III and led us to the topological features of Sec. V and the emergent information entropy wave functions of Sec. VI. The existence

of such signals that can be recovered from data from many distinct physical systems but are hard to conceptualize from sheer theoretical reasoning provides a clear example of how machine learning and model explainability can be important tools in the investigation of quantum materials.

The accuracy scores obtained in the numerical experiments performed in this paper were comparable to those reported in [30], where dense and convolutional neural networks were trained on wave-vector space data to predict the winding numbers of SSH Hamiltonians via supervised learning. This high accuracy level serves as a strong evidence that the entropy signatures presented here indeed express where topological information is most readily available in the SSH lattices investigated.

This paper should also be contrasted with [51], where the subject of investigation is the interpretability of neural network models trained to recognize topological phase transitions in some condensed-matter systems. In [51], interesting visualizations are shown demonstrating that the patterns captured by a single-layer feedforward neural network indeed map directly to known physical quantities that are relevant to the problems at hand. We agree that such tasks should be called *model interpretability*, as in that case the authors introspect into their models to make sure that they are learning patterns of physical pertinence to the systems being investigated. In our paper we preferred the term *model explainability*, as we used similar model introspection tools to propose previously unknown concepts and properties of the physical systems being investigated. While the nuances in the semantics of these two terms are the subject of often heated philosophical debates in the artificial intelligence community, this choice of nomenclature suits the practical application of these model introspection techniques to physics well.

Recent works have demonstrated the existence of local topological markers in real space that carry important information on the topological state of a system [52,53]. Given the DCT and DST topological features introduced in Sec. V which were shown to carry relevant topological information and the theoretical interpretation of the topological signals in terms of information entropy wave functions given in Sec. VI, the results presented here suggest a different road for the theoretical exploration of local topological markers in terms of information theory as well. Whether there is any relationship between the local topological markers of [52,53] and the information entropy wave functions discussed here is left for speculation.

The eigenvector ensembling algorithm employed in this work is likely to have further applications in data-driven physics. This is because most of physics is based on eigenvector decomposition, and statistical physics itself can be seen as an application of similar ensembling principles.

As a concrete example, the study of several many-body systems of current interest in condensed-matter physics is hindered by their large dimensionality. This problem, known as *the curse of dimensionality* in the scientific computing community, arises from the necessity of collecting or processing exponentially larger amounts of data as the feature space dimensionality of a problem grows. An approach based on eigenvector ensembling can be of use in such situations both as a dimensionality reduction tool and as a sampling

strategy. The first case was illustrated in this work, where it was shown that relevant topological information of SSH systems can be retrieved from few sites in a lattice, which can be exploited as a dimensionality reduction strategy. The latter case, which was not explored here, also poses interesting possibilities, such as sampling eigenstates according to a desired distribution in Monte Carlo simulations of condensed-matter systems. Indeed, sampling eigenvectors from a carefully designed probability distribution can ultimately lead to a great reduction in dimensionality while still capturing all the relevant physics of a system. We therefore expect that a much broader class of data-driven physics problems could benefit from the techniques described in this paper.

Another interesting prospect is the combination of eigenvector ensembling with unsupervised learning algorithms. In the paper, our preference for decision trees and random forests was based on their powerful and accessible model explainability aptitudes. This choice was made in conformity with our main purpose, which was to exploit model explainability tools to investigate how topological information is distributed along a spatial lattice in SSH systems. Nevertheless, the eigenvector ensembling procedure we described here is flexible and can easily be repurposed for other supervised or unsupervised learning tasks.

One final comment should be made about the flourishing relationship between physics and machine learning. In this work we have demonstrated how a machine learning approach can provide insights into complex physical phenomena of current interest. The other direction of this relationship (physics enhancing understanding in machine learning) is equally important. As the need for ever more powerful machine learning

algorithms continues to grow, the development of mathematical frameworks for understanding general data spaces (i.e., a physics of data) will be of crucial relevance. This pursuit is seen in many theoretical works investigating the intriguing connections between geometry, topology, and data [54–58]. The detailed study of data generated by physical models with nontrivial geometrical and topological properties such as the SSH model may provide invaluable insights into the structure and shape of real-world high-dimensional data, since these models usually underscore well-known mathematical frameworks behind the data generating process, a feature that is often absent from machine learning applications. Thus, far from being restricted to applications in physics, the study of the topological and geometrical properties of data sets generated by physical models will also be of great value to the machine learning and artificial intelligence communities.

ACKNOWLEDGMENTS

We thank S. E. Rowley, J. F. de Oliveira, T. Micklitz, and M. A. Continentino for insightful discussions and S. E. Rowley for carefully reading the manuscript and suggesting improvements. N.L.H. acknowledges financial support from CENPES/Petrobrás/CBPF. M.A.R.G. acknowledges financial support from **Capes**. N.L.H. is grateful to the Theory of Condensed Matter and Quantum Materials groups at the Cavendish Laboratory and the Quantum Information Group at CBPF.

The authors declare no competing financial or nonfinancial interests.

N.L.H. and M.A.R.G. contributed equally to this work.

- [1] M. Z. Hasan and C. L. Kane, *Rev. Mod. Phys.* **82**, 3045 (2010).
- [2] M. A. Continentino, *Phys. B (Amsterdam)* **505**, A1 (2017).
- [3] T. O. Puel, P. D. Sacramento, and M. A. Continentino, *Phys. Rev. B* **95**, 094509 (2017).
- [4] M. A. Griffith and M. A. Continentino, *Phys. Rev. E* **97**, 012107 (2018).
- [5] S. Ryu, A. P. Schnyder, A. Furusaki, and A. W. Ludwig, *New J. Phys.* **12**, 065010 (2010).
- [6] M. Atala, M. Aidelsburger, J. T. Barreiro, D. Abanin, T. Kitagawa, E. Demler, and I. Bloch, *Nat. Phys.* **9**, 795 (2013).
- [7] B. K. Stuhl, H.-I. Lu, L. M. Ayccock, D. Genkina, and I. B. Spielman, *Science* **349**, 1514 (2015).
- [8] M. Leder, C. Grossert, L. Sitta, M. Genske, A. Rosch, and M. Weitz, *Nat. Commun.* **7**, 13112 (2016).
- [9] N. Goldman, J. Budich, and P. Zoller, *Nat. Phys.* **12**, 639 (2016).
- [10] E. J. Meier, F. A. An, and B. Gadway, *Nat. Commun.* **7**, 13986 (2016).
- [11] M. Hafezi, S. Mittal, J. Fan, A. Migdall, and J. Taylor, *Nat. Photonics* **7**, 1001 (2013).
- [12] L. Lu, J. D. Joannopoulos, and M. Soljačić, *Nat. Phys.* **12**, 626 (2016).
- [13] V. Peano, C. Brendel, M. Schmidt, and F. Marquardt, *Phys. Rev. X* **5**, 031011 (2015).
- [14] T. Kitagawa, M. A. Broome, A. Fedrizzi, M. S. Rudner, E. Berg, I. Kassal, A. Aspuru-Guzik, E. Demler, and A. G. White, *Nat. Commun.* **3**, 882 (2012).
- [15] F. Cardano, M. Maffei, F. Massa, B. Piccirillo, C. De Lisio, G. De Filippis, V. Cataudella, E. Santamato, and L. Marrucci, *Nat. Commun.* **7**, 11439 (2016).
- [16] E. Flurin, V. V. Ramasesh, S. Hacohe-Gourgy, L. S. Martin, N. Y. Yao, and I. Siddiqi, *Phys. Rev. X* **7**, 031023 (2017).
- [17] A. A. Soluyanov, D. Gresch, Z. Wang, Q. Wu, M. Troyer, X. Dai, and B. A. Bernevig, *Nature (London)* **527**, 495 (2015).
- [18] B. Q. Lv, H. M. Weng, B. B. Fu, X. P. Wang, H. Miao, J. Ma, P. Richard, X. C. Huang, L. X. Zhao, G. F. Chen, Z. Fang, X. Dai, T. Qian, and H. Ding, *Phys. Rev. X* **5**, 031013 (2015).
- [19] W. P. Su, J. R. Schrieffer, and A. J. Heeger, *Phys. Rev. Lett.* **42**, 1698 (1979).
- [20] See Supplemental Material at <http://link.aps.org/supplemental/10.1103/PhysRevB.xx.xxxxxx> for further discussions on the SSH model as well as the mathematical feasibility of learning topological phases from real-space data.
- [21] M. Maffei, A. Dauphin, F. Cardano, M. Lewenstein, and P. Massignan, *New J. Phys.* **20**, 013023 (2018).
- [22] A. J. Heeger, *Rev. Mod. Phys.* **73**, 681 (2001).
- [23] C. Kane and T. Lubensky, *Nat. Phys.* **10**, 39 (2014).
- [24] B. G.-g. Chen, N. Upadhyaya, and V. Vitelli, *Proc. Natl. Acad. Sci. U. S. A.* **111**, 13004 (2014).
- [25] J. Carrasquilla and R. G. Melko, *Nat. Phys.* **13**, 431 (2017).
- [26] K. Ch'ng, J. Carrasquilla, R. G. Melko, and E. Khatami, *Phys. Rev. X* **7**, 031038 (2017).
- [27] L. Wang, *Phys. Rev. B* **94**, 195105 (2016).

- [28] P. Broecker, J. Carrasquilla, R. G. Melko, and S. Trebst, *Sci. Rep.* **7**, 8823 (2017).
- [29] E. P. Van Nieuwenburg, Y.-H. Liu, and S. D. Huber, *Nat. Phys.* **13**, 435 (2017).
- [30] P. Zhang, H. Shen, and H. Zhai, *Phys. Rev. Lett.* **120**, 066401 (2018).
- [31] N. Sun, J. Yi, P. Zhang, H. Shen, and H. Zhai, *Phys. Rev. B* **98**, 085402 (2018).
- [32] P. Suchsland and S. Wessel, *Phys. Rev. B* **97**, 174435 (2018).
- [33] Y. Zhang and E.-A. Kim, *Phys. Rev. Lett.* **118**, 216401 (2017).
- [34] J. Venderley, V. Khemani, and E.-A. Kim, *Phys. Rev. Lett.* **120**, 257204 (2018).
- [35] T. Ohtsuki and T. Ohtsuki, *J. Phys. Soc. Jpn.* **86**, 044708 (2017).
- [36] N. Yoshioka, Y. Akagi, and H. Katsura, *Phys. Rev. B* **97**, 205110 (2018).
- [37] D.-L. Deng, X. Li, and S. Das Sarma, *Phys. Rev. B* **96**, 195145 (2017).
- [38] P. Huembeli, A. Dauphin, and P. Wittek, *Phys. Rev. B* **97**, 134109 (2018).
- [39] D. Carvalho, N. A. García-Martínez, J. L. Lado, and J. Fernández-Rossier, *Phys. Rev. B* **97**, 115453 (2018).
- [40] Y. Zhang, R. G. Melko, and E.-A. Kim, *Phys. Rev. B* **96**, 245119 (2017).
- [41] J. F. Rodríguez-Nieva and M. S. Scheurer, *Nat. Phys.* **15**, 790 (2019).
- [42] L. H. Gilpin, D. Bau, B. Z. Yuan, A. Bajwa, M. Specter, and L. Kagal, in *2018 IEEE 5th International Conference on Data Science and Advanced Analytics (DSAA)* (IEEE, Piscataway, NJ, 2018), pp. 80–89.
- [43] F. K. Došilović, M. Brčić, and N. Hlupić, in *2018 41st International Convention on Information and Communication Technology, Electronics and Microelectronics (MIPRO)* (IEEE, Piscataway, NJ, 2018), pp. 0210–0215.
- [44] R. Roscher, B. Bohn, M. F. Duarte, and J. Garcke, *IEEE Access* **8**, 42200 (2020).
- [45] J. Friedman, T. Hastie, and R. Tibshirani, *The Elements of Statistical Learning* (Springer, New York, 2001).
- [46] F. Pedregosa, G. Varoquaux, A. Gramfort, V. Michel, B. Thirion, O. Grisel, M. Blondel, P. Prettenhofer, R. Weiss, V. Dubourg, J. Vanderplas, A. Passos, D. Cournapeau, M. Brucher, M. Perrot, and E. Duchesnay, *J. Machine Learning Res.* **12**, 2825 (2011).
- [47] L. Buitinck, G. Louppe, M. Blondel, F. Pedregosa, A. Mueller, O. Grisel, V. Niculae, P. Prettenhofer, A. Gramfort, J. Grobler, R. Layton, J. VanderPlas, A. Joly, B. Holt, and G. Varoquaux, in *ECML PKDD Workshop: Languages for Data Mining and Machine Learning* (Springer, Berlin, 2013), pp. 108–122.
- [48] L. Breiman, J. Friedman, C. J. Stone, and R. A. Olshen, *Classification and Regression Trees* (Chapman and Hall, London, 1984).
- [49] L. Breiman, *Machine Learning* **45**, 5 (2001).
- [50] L. E. Raileanu and K. Stoffel, *Ann. Math. Artif. Intell.* **41**, 77 (2004).
- [51] Y. Zhang, P. Ginsparg, and E.-A. Kim, *Phys. Rev. Res.* **2**, 023283 (2020).
- [52] R. Bianco and R. Resta, *Phys. Rev. B* **84**, 241106(R) (2011).
- [53] M. D. Caio, G. Möller, N. R. Cooper, and M. Bhaseen, *Nat. Phys.*, 1 (2019).
- [54] G. Carlsson, *Bulletin Am. Math. Soc.* **46**, 255 (2009).
- [55] L. Wasserman, *Annu. Rev. Stat. Appl.* **5**, 501 (2018).
- [56] J. Wang, Z. Zhang, and H. Zha, *Advances in Neural Information Processing Systems* (MIT Press, Cambridge, MA, 2005), pp. 1473–1480.
- [57] T. Lin and H. Zha, *IEEE Trans. Pattern Anal. Machine Intell.* **30**, 796 (2008).
- [58] M. Belkin, *Problems of Learning on Manifolds* (The University of Chicago Press, Chicago, 2003).
- [59] J. K. Asbóth, L. Oroszlány, and A. Pályi, *Lect. Notes Phys.* **919** (2016).
- [60] I. Goodfellow, Y. Bengio, and A. Courville, *Deep Learning* (MIT Press, Cambridge, MA, 2016).
- [61] C. M. Bishop, *Pattern Recognition and Machine Learning* (Springer, New York, 2006).
- [62] L. Cayton, Univ. California San Diego Technical Report No. 12, 2005 (unpublished).
- [63] H. Narayanan and S. Mitter, *Advances in Neural Information Processing Systems* (MIT Press, Cambridge, MA, 2010), pp. 1786–1794.
- [64] S. Rifai, Y. N. Dauphin, P. Vincent, Y. Bengio, and X. Muller, *Advances in Neural Information Processing Systems* (MIT Press, Cambridge, MA, 2011), pp. 2294–2302.